ADVANCED FUNCTIONAL MATERIALS
www.afm-journal.de

Hierarchical Flower Array NiCoOOH@CoLa-LDH Nanosheets for High-Performance Supercapacitor and Alkaline Zn Battery

Ding Zhang, Ying-jie Hua, Xiao-man Fu, Chun-yu Cheng, De-meng Kong, Mei-ling Zhang, Bing-Xin Lei,* and Zhao-Qing Liu**

Nickel oxyhydroxide based energy storage materials have been largely confined by insufficient exposure of active sites which results in low energy efficiency and poor stability. In order to resolve the problems, hierarchical flower array heterostructure NiCoOOH@CoLa-LDH (denoted as NC@CL) nanosheets are designed with NiCo oxyhydroxide (NiCoOOH, denoted as NC) being tightly covered on CoLa layered double hydroxide (CoLa-LDH, denoted as CL) nanosheet. This rational design creates more active sites, enlarges the electrode-electrolyte contact area, improves electron conductivity, and prevents agglomeration during the cycling charge–discharge processes. Density functional theory calculations and differential charges concurrently illustrate that heterostructure formation optimizes the reaction kinetics and promotes electron redistribution. Benefiting from the heterogeneous structure and rich electro-active sites caused by NC, NC@CL displays outstanding reversible specific capacitance (3228 F g^{-1} at 1 A g^{-1}). The aqueous rechargeable alkaline Zn battery NC@CL//Zn exhibits a high capacity of 381.1 mA h g^{-1} at 0.5 A g^{-1} and cycling durability (98% capacity retention after cycling at 5 A g^{-1} for 2000 cycles). The excellent electrochemical performances indicate that NC@CL has great application potential as electrode material for aqueous energy storage device.

1. Introduction

The gradual depletion of fossil energy and serious environmental pollution have greatly hindered the development of human society, stimulated people to develop clean and sustainable energy systems including hydrogen, windy, solar, and tidal powers.[1] In order to ensure the stability and continuity of energy supply, energy storage devices such as chemical batteries have become essential bridge equipment.[2] Although commercial lithium ions batteries have many advantages such as wide electrochemical window, high energy density, stable performance, the shortage of lithium resources, environmental unfriendliness and safety issues have greatly retarded its further application.[3] Supercapacitors made of battery-type electrode materials obtain large energy density and show great application potential.[4] Additionally, alkaline Ni-Zn batteries have also been extensively studied due to their high theoretical capacity, high output voltage, and intrinsic safety, which stem from their similar positive reaction to supercapacitors.[5] Nickel oxyhydroxides and corresponding layer double hydroxides (LDHs)[6] have been potential cathode materials for supercapacitor and Ni-Zn batteries due to their high theoretical specific capacitance and electrochemical reversibility in alkaline solution.[7] However, the limited energy density caused by the low utilization efficiency of nickel cathode is one of the basic bottlenecks of nickel oxyhydroxides electrodes.[8] In addition, under the condition of strong alkali, nickel oxyhydroxide is easy to change the crystal shape and reduce the electrical conductivity, thus reducing the energy density and power density.[9] Co doping is an effective strategy to

D. Zhang, Y.-jie Hua, X.-man Fu, C.-yu Cheng, D.-meng Kong, M.-ling Zhang
School of Chemistry and Chemical Engineering
Key Laboratory of Electrochemical Energy Storage and Energy Conversion of Hainan Province
Hainan Normal University
Haikou 571158, P. R. China
E-mail: zhangding@hainnu.edu.cn

B.-X. Lei
School of Materials and Environment
Guangxi Key Laboratory of Advanced Structural Materials and Carbon Neutralization
Guangxi Colleges and Universities Key Laboratory of Eco-friendly Materials and Ecological Restoration
Guangxi Minzu University
Nanning 530105, P. R. China
E-mail: leibx@gxmzu.edu.cn

Z.-Q. Liu
School of Chemistry and Chemical Engineering
Institute of Clean Energy and Materials
Key Laboratory for Clean Energy and Materials
Guangzhou University
Guangzhou 510006, P. R. China
E-mail: lzqgzu@gzhu.edu.cn

The ORCID identification number(s) for the author(s) of this article can be found under https://doi.org/10.1002/adfm.202414686

DOI: 10.1002/adfm.202414686

improve the stability of nickel oxyhydroxides in alkaline solution.[10] However, the applications of nickel-cobalt oxyhydroxides based electrodes are still hampered due to their insufficient active site and low electron conductivity.[10b,e,11]

An optimized integration of NiCoOOH with other electroactive materials to create heterostructure architectures is seen as a promising solution for addressing the aforementioned issues.[12] Through the rational design and assembly of two constituents, the hierarchical heterostructure architectures not only provide more electroactive sites but also foster significant synergies between the active materials thus expediting redox reactions.[13] Additionally, the hierarchical heterostructure architectures possess high mechanical strength and a highly open porous morphology, greatly enhancing the specific surface area and improve electrical conductivity.[14] Crucially, the active centers may undergo reconstruction at the interface due to robust interactions between various components, thereby amplifying the intrinsic activity of hybrid electrocatalysts.[10e,15]

In this paper, $Co(OH)_2$ doped with La is selected as the base material for heterostructure construction due to $Co(OH)_2$'s high theoretical specific capacitance, robust electrical conductivity, and good stability,[16] combined with La's unique physicochemical properties arising from its localization and incomplete filling of the 4f band.[17] The assembled asymmetric supercapacitors NC@CL//AC displayed approving specific capacitance (213 F g^{-1} at 0.2 A g^{-1}) and cycling property (88.1% capacitance retention after 20 000 cycles). The aqueous rechargeable alkaline Zn battery NC@CL//Zn exhibits a high capacity of 381.1 mA h g^{-1} at 0.5 A g^{-1} and cycling durability (98% capacity retention after cycling at 5 A g^{-1} for 2000 cycles).

2. Results and Discussion

2.1. Morphology and Structure

The single factor method was used to optimize the ratios of Co:La, Ni:Co, and NC:CL. Detailed optimization experiments are displayed in the Supporting Information. As shown in Figure S1 (Supporting Information), the CV and GCD results exhibit that the optimal ratio of Ni: Co is 3:1 for NC electrodes and Co:La is 10:1 for CL electrodes. As shown in Figure S2 (Supporting Information), sample 3 exhibits the largest CV areas and longest discharge time for this NC and CL ratio, indicating the best electrochemical energy storage capacity in this NC:CL ratio. This indicates that NC and CL achieve better synergistic energy storage effect under the NC:CL ratio of sample 3. The NC, CL, and NC@CL samples for subsequent preparation and detection were all prepared under optimal conditions.

The preparation processes are demonstrated in **Figure 1a**. The CL was synthesized by hydrothermal method initially. The obtained CL exhibits smooth, flower-like nanosheets replete with porous structures as displayed in Figures 1b–d and S3a (Supporting Information). The porous CL nanosheet was used as substrate and added into the Teflon-lined autoclave by next hydrothermal reaction with 120 °C for 3 h. For comparison, pure NC materials have also been prepared by hydrothermal reaction and displayed in Figure S3b–e (Supporting Information). After being coated with NC, the initially smooth CL nanosheets underwent coarsening as depicted in Figures 1e–g and S3f (Supporting Information). The rough nanosheets interconnect with each other, forming a 3D hierarchical network architecture with ultrathin sheet thickness (Figure 1e–g). This structure not only prevents large number of active sites but also provides large electrode-electrolyte interfaces and sufficient ion diffusion channels.

The porous properties of the as-prepared CL, NC and NC@CL samples were tested by nitrogen adsorption-desorption analysis. The isothermal curve of adsorption-desorption and pore size distribution (PSD) curves obtained from their corresponding desorption branches using the Barrett-Joyner-Halenda (BJH) method are shown in Figure S4 (Supporting Information). The calculated results shows that the BET surface of NC@CL, NC, and CL samples was 316.4, 237.8, and 121.8 m^2 g^{-1}, respectively. Upon comparing NC and CL at an equivalent scale (as depicted in Figure S3a,b, Supporting Information), it is observed that NC exhibits a nanosheet structure characterized by reduced dimensions and an elevated pore density. Consequently, NC possesses a greater specific surface area and a narrower pore size distribution. The enhanced BET surface of NC@CL indicates that the coated NC component increases the specific surface area of CL. The three samples displayed type IV isotherms with distinct hysteresis loops at the relative pressure between 0.3 and 1.0, demonstrated the existence of mesoporous structures. As shown in the pore size distribution curves, the CL possessed bigger pores of 50 nm and the NC@CL and NC obtained two main ranges of the smaller pores (2–10 nm) and the bigger pores (>10 nm).

The consensus was that macropores (>50 nm) acted as electrolyte reservoirs, mesopores (2–50 nm) aided in exposure more active sites, whereas smaller mesopores (2–5 nm) and micropores (<2 nm) amplified the ion-accessible surface area, thereby playing a substantial role in capacitance enhancement.[18] After being coated with NC, the NC@CL heterostructure exhibited a higher proportion of advantageous mesopores within the 2–5 nm range (refer to Figure S4b, Supporting Information). This resulted in the creation of additional surface electroactive sites and shorten the ion-accessible surface area, thereby facilitating rapid redox reactions and enhancing both energy density and power capability.[11b,19]

The structural features of NC@CL nanosheets were further investigated by transmission electron microscope (TEM) and High-resolution TEM (HRTEM). Figure 1a shows the crystal structure diagram of NC@CL. It can be found that the upper NC regular octahedral structure was connected with lower CL octahedral structure by the La-O bonds which shows twisted octahedral structure. **Figures 2a** and S5 (Supporting Information) confirmed the layered stacking structure of NC@CL. The corresponding energy dispersive spectroscopy (EDS) mapping in Figure 2b demonstrates homogeneous distribution of Ni, Co, La and O elements among NC@CL nanosheets. The HRTEM images (Figure 2c–e) displayed the lattice fringe with spacing of 0.260 and 0.211 nm, which can be attributed to the (101) plans of CL and (105) plane of NC.[20] And the corresponding selected area electron diffraction (SAED) pattern (insert of Figure 2c) reveals a polycrystalline feature of NC@CL nanosheets. As displayed in the Figure 2f,g, the lattice fringe spacing (105) plane of NC and (101) plans of CL were larger than the standard value of NC (0.209 nm) and CL (0.237 nm), proving the existence of lattice deformation. The

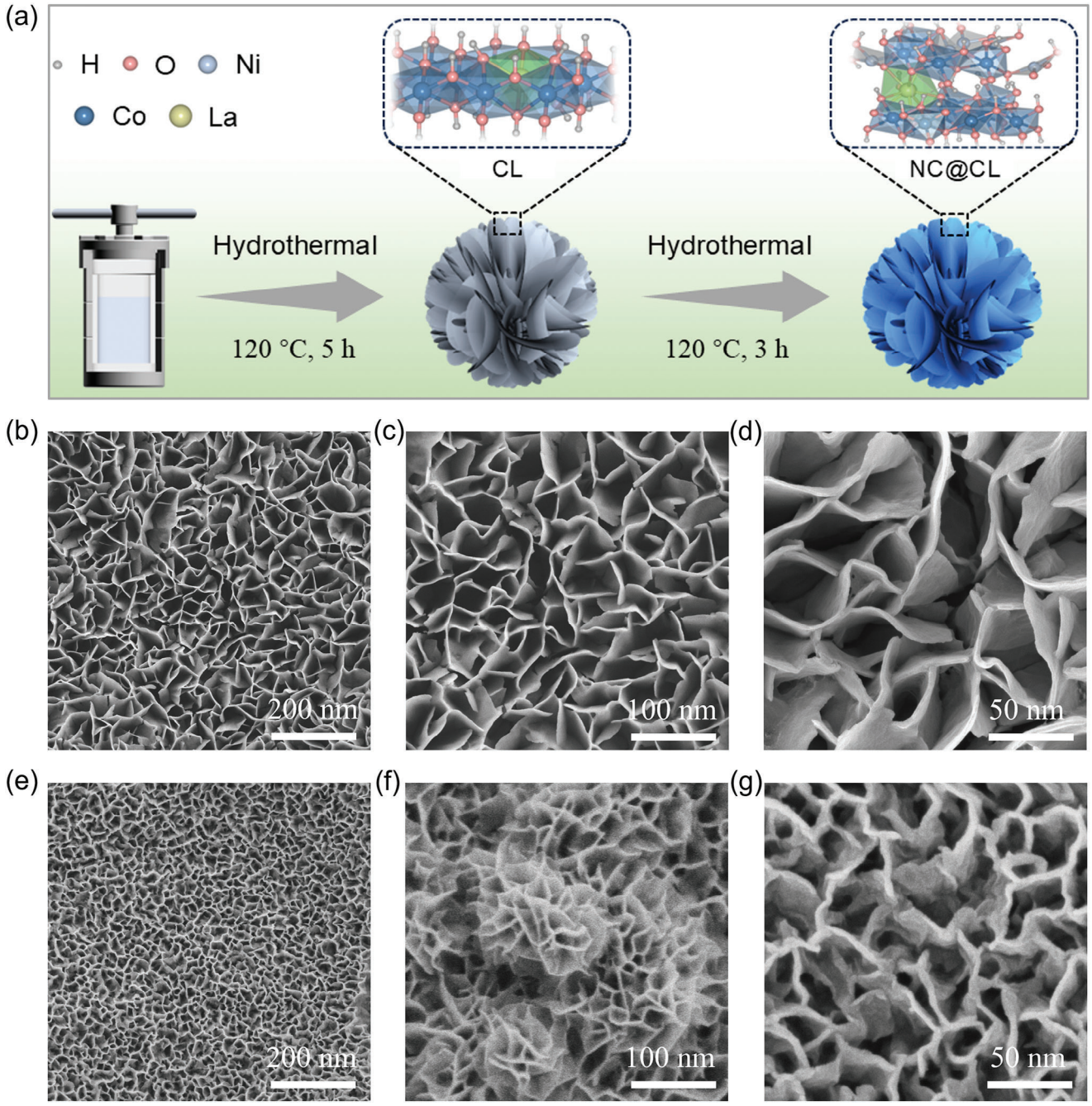

Figure 1. a) Schematic illustration for synthesis process of NC@CL nanosheet arrays. b–d) Scanning electron microscope (SEM) images of CL nanosheet. e–g) SEM images of hierarchical flower-like array NC@CL nanosheet.

possible rationale is that the incorporation of lanthanum, possessing a substantial ionic radius (1.06 Å), occupies cobalt (ionic radius 0.745 Å) sites within the octahedral $Co(OH)_2$, leading to lattice distortion. Additionally, the formation of the NC@CL heterojunction introduces interfacial stress, further exacerbating lattice deformation in both NC and CL. This lattice deformation fine-tunes the diffusion behavior of electrons and ions within the crystal structure, optimizing transport pathways and rates, thereby accelerating the charge transfer process. Concurrently, it effectively modulates grain boundary interface reactions, enhancing the adsorption and desorption dynamics of reactants on the electrode surface, ultimately optimizing interface reaction kinetics. The TEM image of NC@CL confirms that interconnected ultrathin nanosheets were formed as building blocks for assembling the nanoflowers replace nanocrystallines. Obviously, 3D layered nanostructure shortens the distance between electrolyte ions and the reaction active site, thus promoting the overall utilization of electroactive materials. As expected for

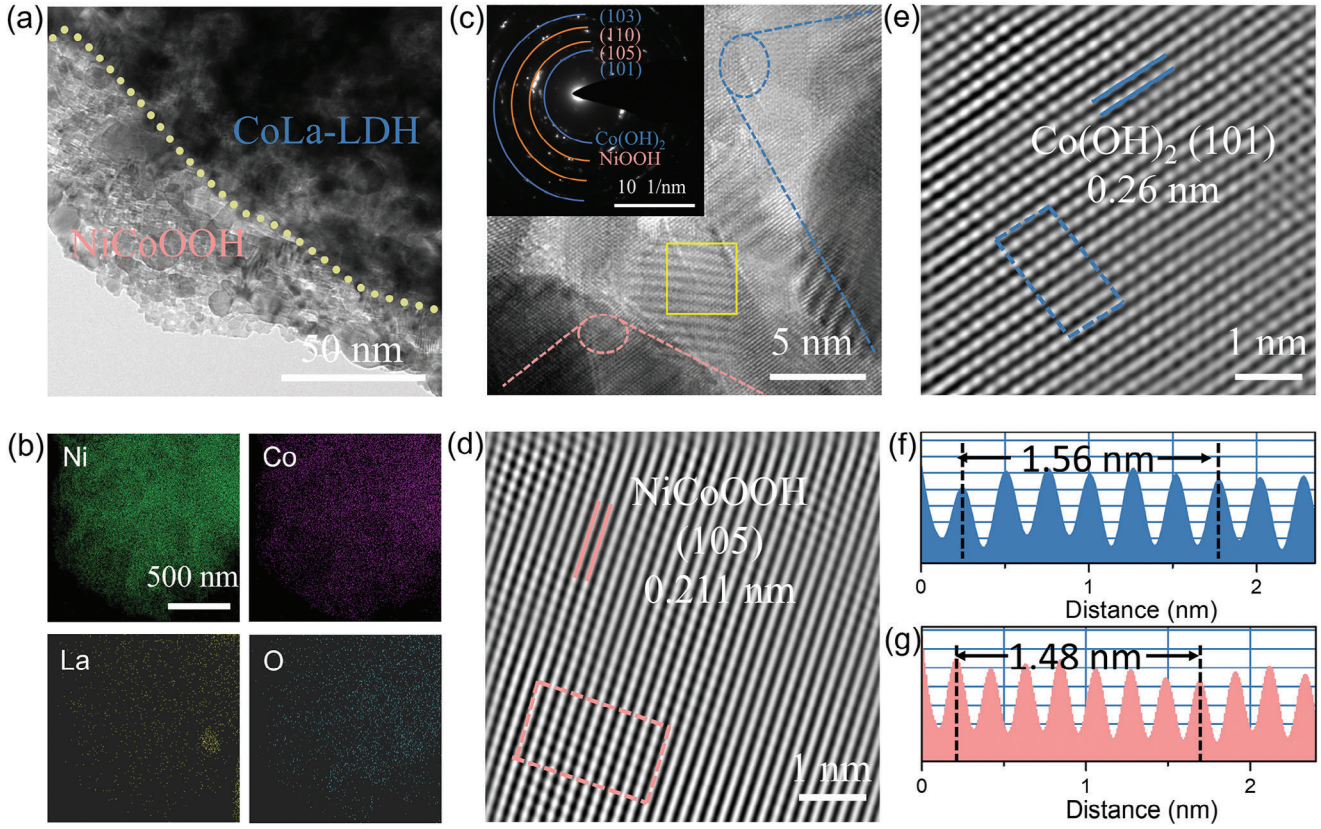

Figure 2. a) TEM, b) EDS, and c–e) HRTEM images of NC@CL nanosheets; insert of (c) is the corresponding selected area electron diffraction (SAED) pattern from yellow dotted box in (c). f,g) Intensity distribution measured from the crystal spacing of HRTEM images.

material design, the above results confirm that nanosheet architecture was constructed successfully by the two steps hydrothermal treatment.

X-ray diffraction (XRD) and X-ray photoelectron spectrometer (XPS) were conducted to determine the phase compositions and the surface electronic states in as-prepared NC@CL nanosheet. As displayed in the **Figure** 3a, the XRD pattern of CL substrate and pure NC can be accordingly indexed to the hexagonal $Co(OH)_2$ (JCPDS No. 30–0443) and hexagonal NiOOH (JCPDS No. 06–0075), respectively. After coating of NC layer on the CL substrate, a mixture diffraction peaks of hexagonal $Co(OH)_2$ (JCPDS No. 30–0443) and hexagonal NiOOH (JCPDS No. 06–0075) can be found for the NC@CL nanosheet sample. This indicated that the composite NC@CL nanosheet obtained a mixed crystal structure.

XPS testing was conducted to further confirm the chemical states of the NC@CL heterojunction and to investigate the electronic interactions between the two components of the heterostructure. The Co 2p high-resolution spectrum (Figure 3b) exhibited two distinguished peaks located at 775.6 and 781.1 eV corresponding to Co^{3+} and Co^{2+}, respectively.[21] The main Co^{2+} indicated that cobalt exists in the form of $Co(OH)_2$.[22] As displayed in the Ni 2p high-resolution spectrum (Figure 3c), typical peaks consistent well with Ni 2p1/2 and Ni 2p3/2 levels can be found.[23] After fitting, the Ni 2p3/2 spectrum displayed two predominant Ni species, i.e., Ni^{3+} (855.6 eV) and Ni^{2+} (852.1 eV), suggesting two valence states of Ni in the material.[24] The dominant Ni^{3+} indicates that NC was obtained. When compared to NC and NC@CL, the emergence of Ni^{2+} within NC@CL suggests that the presence of inferior CL influences the reaction during the secondary hydrothermal synthesis of the heterojunction. Specifically, the heterogeneous interface between CL and NC results in electron migration to NC, which may be responsible for the generation of Ni^{2+} in NC@CL. The Co 2p and Ni 2p spectra of the NC@CL heterostructure exhibited a slight downward shift in comparison to those of pure NC and CL. This shift indicates strong electronic interactions between the CL and the NC via established epitaxial heterogeneous interfaces.[25] For the La 3d high-resolution spectrum (Figure 3d), it can be deconvoluted into two main peaks at 835.2 eV and 851.8 eV corresponding to 3d5/2 and 3d3/2 spin orbit, which are assigned to La^{3+}[26] Notably, the binding energy of La 3d for NC@CL heterostructure showed a positive shift of 0.4 eV in comparison with pure CL, also demonstrating the strong interaction between CL and the NC.[27] The O 1s high-resolution spectrum are shown in Figure 3e, the deconvoluted results demonstrated that the main oxygen contribution is OH^-/OOH^- groups. There are no obvious M-O and absorbed water in the O 1s spectrum. All of these results demonstrate that the NC@CL heterojunction is synthesized with CL and NC. The electron-localization function plots of NC@CL (Figure 3f) suggest the presence of La-O bonds. The strong interfacial interaction not only customized the surface electronic structure but also hastened electron transfer within the NC@CL heterostructure which enhanced the kinetics

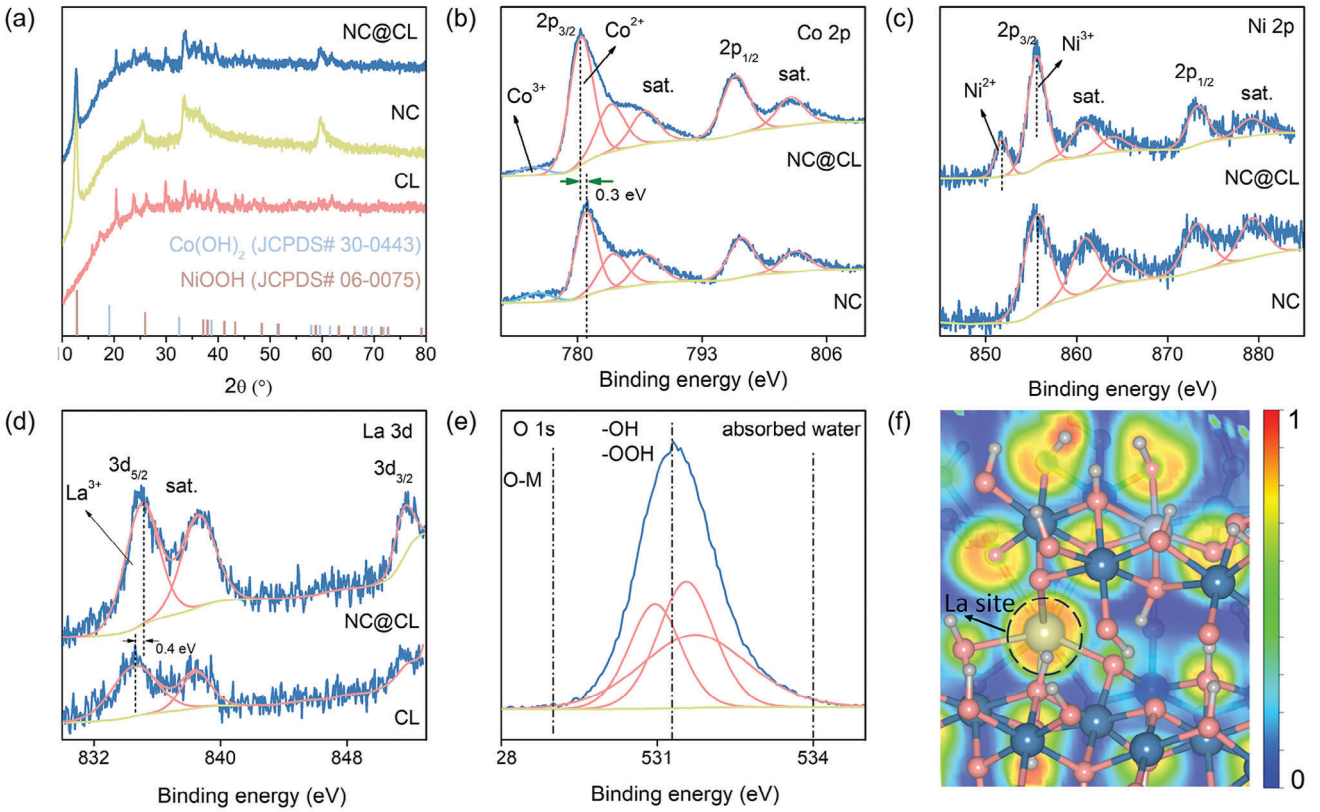

Figure 3. a) XRD patterns of NC@CL nanosheet, CL, and single NC samples. The high-resolution XPS spectra of b) Co 2p and c) Ni 2p, d) La 3d, and e) O 1s of NC@CL heterostructure, respectively. f) Electron localization function of NC@CL heterostructure.

of the redox reaction, ultimately enhancing the electrochemical process.[25,28]

2.2. The Electrochemical Performance of NC@CL Nanosheet Electrodes for Supercapacitor

The electrochemical measurements were conducted in three-electrode system in 2 mol L^{-1} KOH electrolyte for single electrode to analyze the electrochemical behaviors in supercapacitors. **Figure** 4a displayed the cyclic voltammetry (CV) curves of NC, CL, and NC@CL at the scan rate of 5 mV s^{-1} in a potential range from −0.2 to 0.6 V (vs Ag/AgCl). All the curves of the three electrodes show obvious redox peaks, that differ from the ideal rectangular of double-layer capacitance, indicating the pseudocapacitive feature of NC, CL, and NC@CL electrodes. Among them, the integrated area of CV curves for NC@CL heterostructure are largest, indicating highest capacitance of it. The galvanostatic charge/discharge (GCD) curves of the three symmetric supercapacitors NC//NC, CL//CL, and NC@CL//NC@CL at 1 A g^{-1} in the potential window of 0–0.5 V (vs Ag/AgCl) are shown in Figure 4b. The NC@CL electrode possesses longer discharge time and higher capacitance, which is in line with CV results.

The charge storage ability of the electrodes is further evaluated by conducting GCD at different current densities. The CV and GCD curves of NC//NC, CL//CL and NC@CL//NC@CL at varied current densities are tested and shown in Figure S6 (Supporting Information) and Figure 4c, respectively. The obvious potential plateaus of the three electrodes further certify the pseudocapacitive characteristic of NC, CL, and NC@CL electrodes. The GCD curves of the three electrodes display good symmetry at various current densities that imply good charge/discharge coulombic efficiency of the electrodes. The specific capacity of three electrodes at current densities of 1, 2, 3, 5, and 10 A g^{-1} were calculated and plotted as a function of current density based on the loading active material mass (Figure 4d). The longer charge and discharge times of NC@CL heterostructure than other electrodes at same current density indicates the higher capacitance of NC@CL electrode. The calculated capacitance of NC@CL electrode is 3228, 2964, 2700, 2360, 1850 F g^{-1} at 1, 2, 3, 5, and 10 A g^{-1}, respectively. Comparing with reported Ni and Co based electrodes, the NC@CL electrode is competitive or outperforms as list in Table S1 (Supporting Information). By co-precipitation method, the NC@CL with nano rod structure was synthesized. The nano rod-like structure and the associated distribution of elements can be observed in the SEM, TEM, and EDS images of Figure S7 (Supporting Information). Both CV and GCD tests prove that the NC@CL electrode with nanosheets structure posses better charge storage performance than nano rod (Figure S8, Supporting Information). The outstanding electrochemical performance of NC@CL electrode can be attributed to three reasons. For one thing, the flower-like nanosheet structure possesses large specific surface area and exposes more active

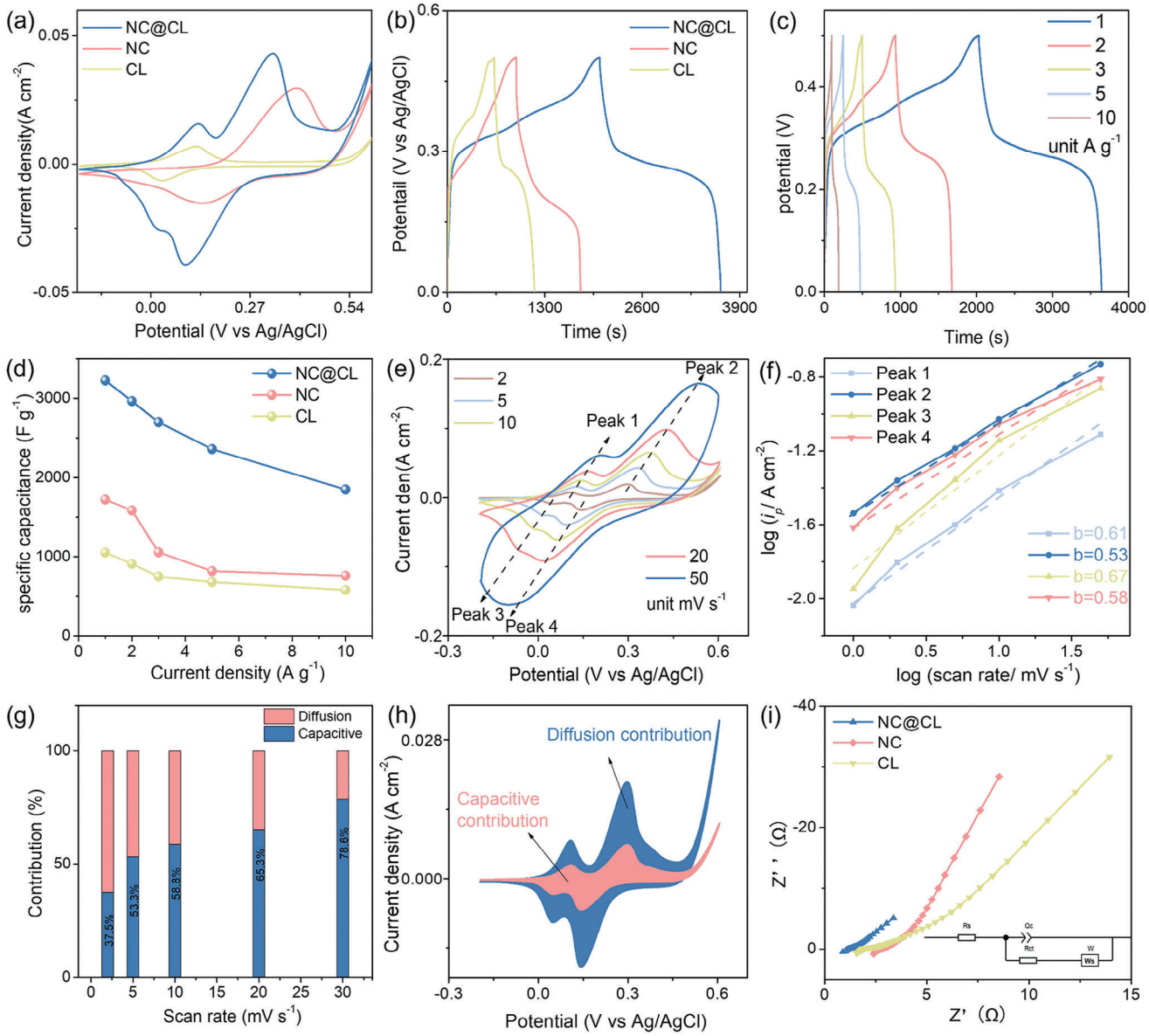

Figure 4. Electrochemical measurements of the NC@CL, CL, and NC electrodes in 2 mol L^{-1} KOH aqueous solution. a) CV curves at 5 mV s^{-1}. b) GCD curves of NC@CL//NC@CL, NC//NC, and CL//CL at 1 A g^{-1}. c) GCD curves of NC@CL//NC@CL symmetric supercapacitor at different current densities. d) The specific capacitance as a function of scan rate. e) CV curves of NC@CL electrode at varied scan rates. f) The peak currents against the scan rates of NC@CL. g) The ratio of capacitive contribution at different scan rates of NC@CL. h) The diffusion-controlled and capacitive contribution at 2 mV s^{-1}. i) EIS Nyquist plots of three samples.

sites which can increase the contact area with the electrolyte and shorten the ion/electron conduction path. In addition, proper ratio of Co:La and Ni:Co can provide more active sites thus effectively improve the capacitive performance of the material. Finally, the construction of heterostructure provides numerous ion transport channels, enhancing the structural strength of the material.[28]

The energy storage mechanism of the NC@CL electrode in supercapacitor is further elucidated by kinetic analysis. The diffusion controlled and capacitive controlled processes in electrochemical testing are distinguished by the Equations (1) and (2) according to the powers law between the peak currents (i) and scan rates (v) of CV curves.[29]

$$i = a\, v^{b} \tag{1}$$

$$log\, i = log\, a + b\, log\, v \tag{2}$$

where, "a" represent adjustable parameters, and the "b" value can be confirmed by the angle of the fitting line (log i versus log v). Theoretically, if the b-value is 0.5, the diffusion controlled (battery-type) behavior is dominant and the b-value of 1

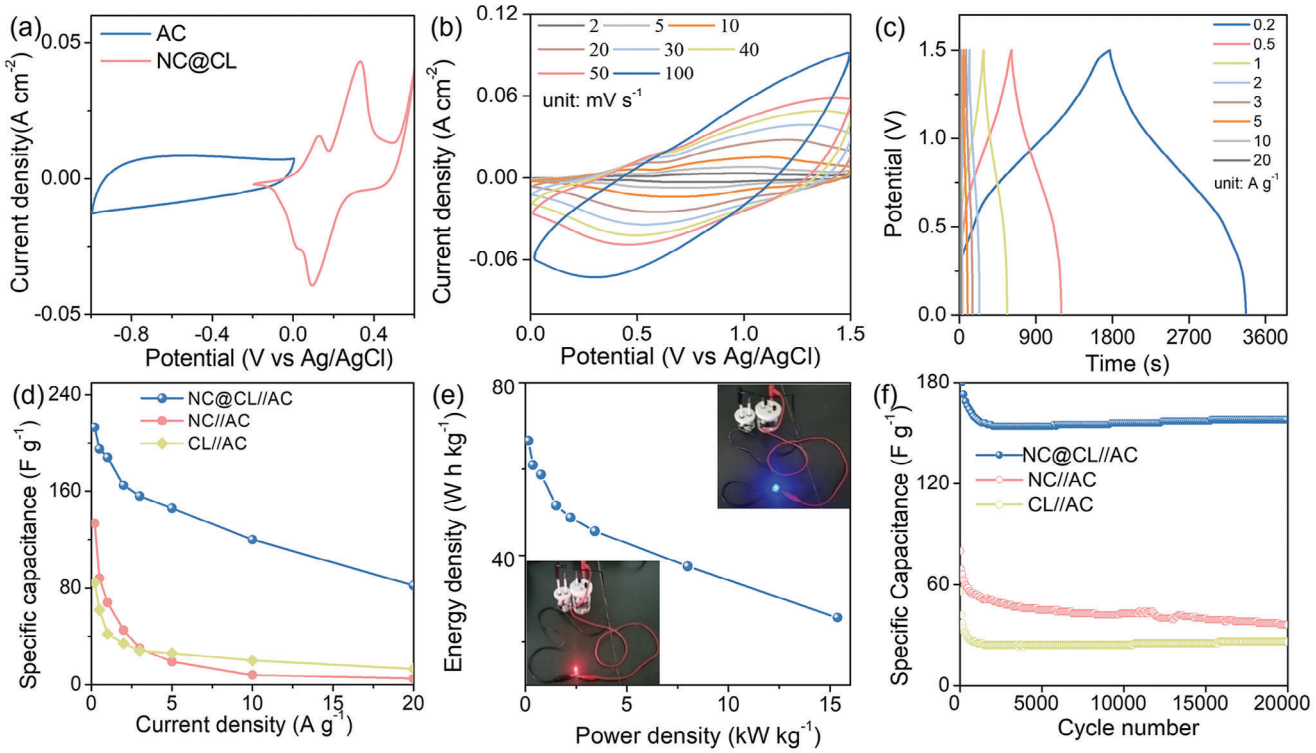

Figure 5. a) Electrochemical measurements of the asymmetric supercapacitor. CV curves of the NC@CL and AC electrode at 5 mV s^{-1} based on three electrode system. b) CV curves of NC@CL//AC ASC at different current densities. c) GCD curves at different current density from 0.2 to 20 A g^{-1} of the NC@CL//AC device. d) The specific capacitances obtained from different current density. e) Ragon plot of NC@CL//AC (insert photograph are red and blue LEDs lighted for several hours by two ASC devices in series). f) Cycling properties of the three devices at 1 A g^{-1}.

represents the surface capacitive confined. The b-values obtained at different oxidation/reduction potentials for the NC@CL electrode are close to 0.5 within the potential range of −0.2 to 0.6 V at scan rate between 2 and 50 mV s^{-1} (Figure 4e,f), implying that the energy storage mechanism is diffusion-controlled processes. The four peaks in Figure 4e represent the Faradaic process of the Ni^{2+}/Ni^{3+} and Co^{2+}/Co^{3+} redox pairs, specifically peaks 1 and 3, can be ascribed to the redox reactions of CL, whereas peaks 2 and 4 are attributable to the redox reactions of NC, as evidenced by a comparative analysis of the CV curves among NC, CL, and NC@CL composites depicted in Figure 4a. The emergence of the four peaks substantiates the participation of both the superior and inferior hierarchical layers in the charge storage reaction, yielding a synergistic effect through their collective interaction.

Moreover, the percentages of surface capacitive-controlled ($k_1 v$) contribution and diffusion-controlled ($k_2 v^{1/2}$) contribution can be further calculated by Equation (3):

$$i\ (v) = k_1\ v + k_2\ v^{1/2} \tag{3}$$

where i (v) represent the current at a specific potential (V). For the NC@CL electrode, the capacitive-controlled contribution was 37.5% at 2 mV s^{-1} (Figure 4g,h). It means that, the electrochemical kinetic processes were diffusion-controlled at low scan rates, for that the electrode materials had enough times for redox reaction, hence showing battery-type behaviors. As the scan rate increases from 2 to 30 mV s^{-1}, the capacitive-controlled contributions gradually enhanced to 78.6%, verifying that NC@CL electrode displayed capacitive-based kinetics behaviors at high scan rates. High proportion of capacitive-controlled contribution makes NC@CL electrode obtain good rate performance. This is mainly attributed to the unique heterogeneous nanostructure of NC@CL electrode, strong interface bonding effects between NC and CL, homogeneously dispersed active materials, and abundant active sites for the surface capacitive reactions.

Figure 4i shows the electrochemical impedance spectroscopy (EIS) Nyquist plots of the NC@CL, NC, and CL in the frequency range from 0.01 to 100 kHz. Obviously, the minimum internal resistance of solution (Rs = 0.7564 Ω) is obtained for NC@CL (NC is 2.31Ω, CL is 1.52 Ω), indicating the fast electron transmission in electrolyte. In addition, the interface charge transfer resistances of NC@CL, NC, and CL electrodes are calculated to be 0.23, 0.447, and 0.43 Ω, respectively. The lower interface charge transfer resistance of NC@CL reveals that the construction of heteronanosheet structure facilitated the OH^- adsorption and reduced the internal resistances.

The asymmetric supercapacitor (ASC) devices are also built up by employing NC, CL and NC@CL as cathode and activated carbon (AC) as anode to investigate their potential applications. The CV curves of single NC@CL and AC (**Figure 5a**) revealed the difference in the voltage window of −0.2–0.6 V (vs Ag/AgCl) and −1–0 V (vs Ag/AgCl), respectively. The rectangular CV curves of AC indicating the characteristic of the electrical double-layer capacitor (EDLC).[30] The mass ratio for the cathode electrodes and

AC electrodes were optimized based on the charge balance regulation: $Q^+ = Q^-$.[31] The subsequent CV curves of the asymmetric NC@CL//AC, NC//AC, and CL//AC supercapacitors at various scan rates from 2 to 100 mV s^{-1} were shown in Figures 5b and S9a,b (Supporting Information) within a potential window of 1.5 V. It can be noted that these CV curves showed a joint pseudocapacitive and EDLCs feature. The shapes of these CV curves hold up well even at 100 mV s^{-1}, indicating excellent capacitive performance of these ASC devices. Figures 5c and S9c,d (Supporting Information) show the GCD curves of the NC@CL//AC, NC//AC and CL//AC devices, respectively. The specific capacitances of three electrodes are calculated from GCD results as displayed in the Figure 5d. The NC@CL//AC exhibits a specific capacitance of 213, 195, 188, 165, 156, 146, 120, and 82 F g^{-1} at 0.2, 0.5, 1, 2, 3, 5, 10, and 20 A g^{-1}, respectively, which is higher than that of NC//AC and CL//AC devices. The original lower resistance and faster electron/ion diffusion into electrode material as demonstrated from EIS plots in Figure S9e (Supporting Information) and Table S2 (Supporting Information) are beneficial to the good capacitive properties of NC@CL.

The Ragon plot of energy versus power density is given in Figure 5e. The NC@CL//AC achieves superior energy density of 66.56 W h kg^{-1} at a power density of 148.83 W kg^{-1}, and 25.63 Wh kg^{-1} even at 15 375 W kg^{-1}, which is competitive than NiCo based devices in reported literatures such as NiCo-LDH@$Ni(OH)_2$//AC (30.6 W h kg^{-1} at 799.9 W kg^{-1}),[11a] CuO@NiCo-LDH//AC (47.3 W h kg^{-1} at 800 W kg^{-1}),[32] Ni_2Co-S//AC (65.2 W h kg^{-1} at 400 W kg^{-1}),[33] $NiCo(CO_3)(OH)_2$//Go (41.1 W h kg^{-1} at 201.2 W kg^{-1}),[34] Se@(NiCo)Se-2//AC (49.4 W h kg^{-1} at 787.3 W kg^{-1}),[35] $Ni_xCo_{3-x}O_4$/NF//AC (39.3 W h kg^{-1} at 800.2 W kg^{-1}).[36] The illuminated light emitting diode (LED) bulb insert in the Figure 5e demonstrates the practicality of the NC@CL//AC supercapacitor. The cycling stability of the NC@CL//AC, NC//AC, and CL//AC devices are assessed by conducting the GCD tests at 1 A g^{-1} (Figure 5f). After 20 000 cycles, the NC@CL//AC keeps 88.1% of capacitance retention, demonstrating the good cycling stability.

2.3. The Electrochemical Performance of NC@CL Nanosheet Electrodes for Alkaline Zn Batteries

To further investigate the practicability, typical aqueous rechargeable alkaline Zn batteries are assembled with NC@CL, NC, and CL as cathodes, 1 M KOH + 5 mM ZnO as electrolyte, and Zn foil as anode. **Figure 6a** shows the CV curves of the three electrodes at 5 mV s^{-1}. As displayed in Figure 6a, the NC@CL//Zn battery obtained larger integrated CV curves area among the three batteries, indicating improved specific capacity of NC@CL//Zn battery. The charge/discharge behavior is compared for the three batteries as shown in Figure 6b, and the discharge capacity for NC@CL//Zn, NiCo-LD//Zn, and CL//Zn at 0.5 A g^{-1} is 381.1, 199.8, and 161.7 mA h g^{-1}, respectively. As expected, the NC@CL electrode delivers longer discharge time, confirming its less polarization and enhanced specific capacity.[11c] The CV curves of NC@CL//Zn, NC//Zn, and CL//Zn batteries at scan rate from 2 to 50 mV s^{-1} are given in Figures 6c and S10a,b (Supporting Information), respectively. And the typical GCD curves of NC@CL//Zn batteries from 0.5 to 10 A g^{-1} are presented in Figure 6d. It can be observed that all of the charge/discharge plots display obvious voltage platform located at ≈1.6 V, which is consistent with the CV curves. In addition, the specific capacity of NC@CL//Zn batteries decrease from 381.1 to 243.4 mA h g^{-1} as current density increases from 0.5 to 10 A g^{-1}. As comparison, the electrochemical behavior of NC//Zn and CL//Zn batteries is also studied (Figure S10c,d, Supporting Information). Figure 6e shows that the average discharge capacity for NC@CL//Zn is 381.1, 354.2, 331.8, 300.6, 294.7, 278.4, 252.5, 234.2 mA h g^{-1} at current density of 0.5–10 A g^{-1}, which is higher than that of NC//Zn and CL//Zn, implying improved electrochemical property of NC@CL//Zn. Moreover, for NC@CL//Zn battery, when the current density is restored to the initial low degree, the discharge capacity is almost maintained at the original level, which confirms its satisfactory rate capability. Comparing with reported NiCo based aqueous Zn battery, the NC@CL//Zn is competitive or outperforms as listed in Table S3 (Supporting Information). The superior rate performances of NC@CL//Zn is mainly ascribed to the low internal resistance and charge transfer resistance, as reflected by the Ragon plots in Figure S10e and Table S4 (Supporting Information).

Figure 6f shows the cycling performance for the three battery devices. For NC@CL//Zn battery the initial lower capacity at the first 200 cycle may be due to electrochemical activation and slowly expose of active sites to electrolyte.[37] Thereafter the capacity increases gradually with the increase of continuous cycles till to 1300 cycle and slightly declines until the end of the test, which is higher than that of NC//Zn and CL//Zn, imping satisfied electrochemical reversibility and cycling durability of the NC@CL//Zn battery (98% capacity retention). To further verify the practical application of fabricated NC@CL//Zn battery, two coin cell devices are connected in series for power sources. As a practical demonstration, the battery can light up different colors of LED lights continuous, as shown in Figure 6g (white, red, blue and yellow LED), demonstrating the great potential in consumer electronic applications. The NC@CL//Zn battery and NC@CL//AC supercapacitor is able to light up the blue and red LDE for hours, respectively. The related video file of illuminating blue and red LED testing is given in supplementary data.

After 2000 cycles tests, the NC@CL, NC and CL//Zn are investigated by SEM, EDS and XPS. The SEM images in Figures S11–S13 (Supporting Information) display that the electrodes subjected to agglomeration and corrosion. For the NC@CL electrode, the flower-array heterogeneous nanosheet structure remains discernible as shown in Figure S11a,b (Supporting Information), indicating its favorable efficacy in mitigating agglomeration. And the corresponding EDS mapping results reveals that all the elements are still distributed uniformly. The valence states of each element of NC@CL are further verified by XPS (Figure S14, Supporting Information). It can be found that the Co, Ni, La, and O element can be detected by XPS and the valence state of them has no obvious change. The stability of the structure and composition ensures the long-term cycle stability of the NC@CL electrode.

The intrinsic mechanisms of enhanced capacity performance of NC@CL nanosheet array is further performed via density functional theory (DFT) calculations. The partial density of states (PDOS) of NC@CL, NC, CL, and $Co(OH)_2$ are plotted to better

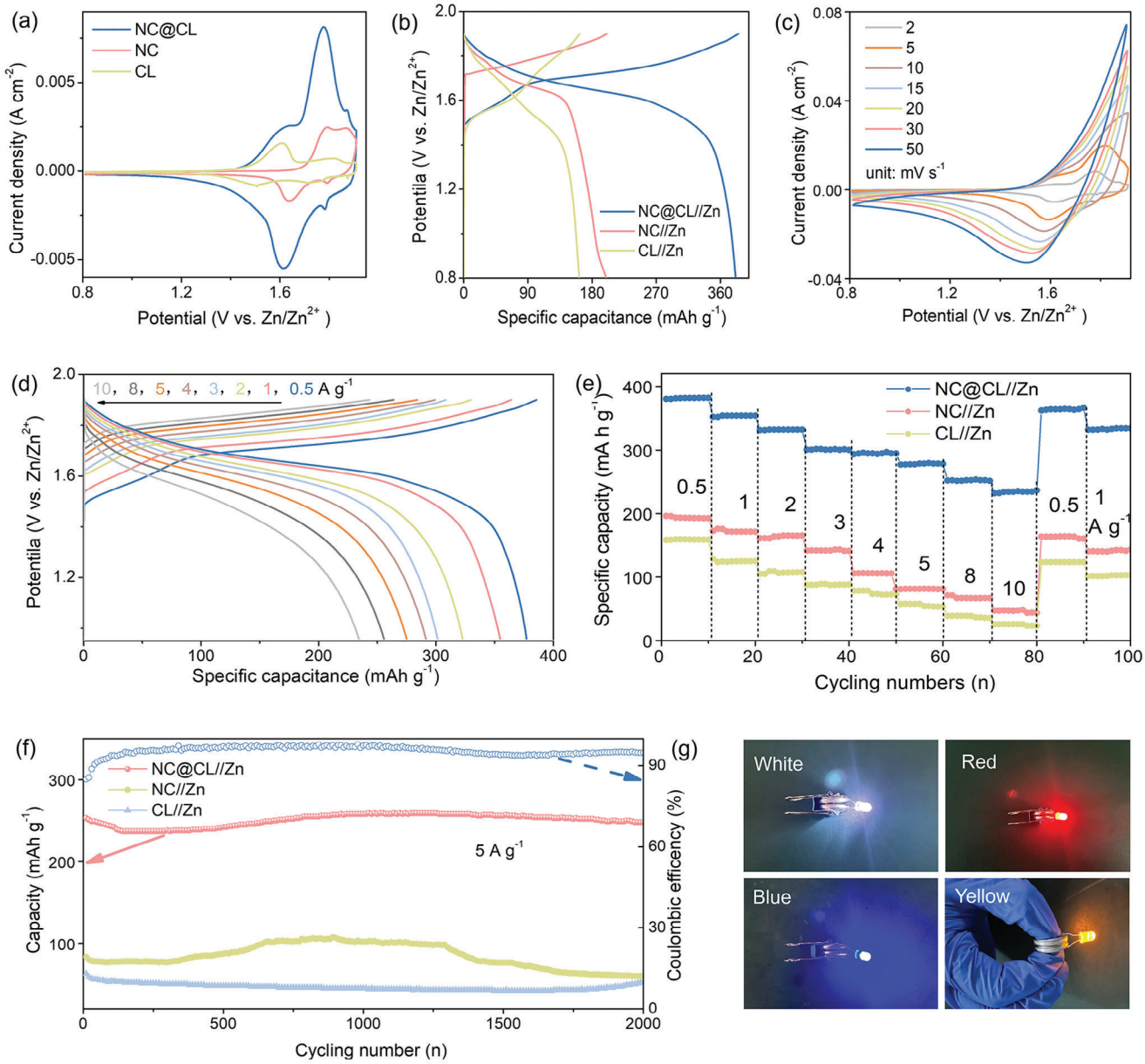

Figure 6. Electrochemical measurements of the aqueous Zn battery. a) Comparison of CV curves of NC@CL//Zn, NC//Zn, and CL//Zn at 5 mV s^{-1}. b) GCD curves of NC@CL//Zn, NC//Zn, and CL//Zn batteries at 0.5 A g^{-1}. c) CV curves of NC@CL//Zn at different current density. d) GCD curves of the NC@CL//Zn battery at different current density. e) Rate performances of three batteries at varied current densities from 0.5 to 10 A g^{-1}. f) Long-time cycling performance at 5 A g^{-1} for 2000 cycle. g) Photo image of LEDs lit up by the assembled NC@CL//Zn batter.

grasp the alternation in electronic structure of NC@CL, shown in **Figure** 7a,b. As observed from the PDOS patterns of CL and $Co(OH)_2$ in Figure 7a, the d-band center of $Co(OH)_2$ is away from the Fermi level than that of CL. This demonstrated that the La optimizes the electron cloud configuration of cobalt and enhances its reactivity.[27b] Further analyzing the PDOS patterns of NC@CL, NC, and CL in Figure 7a,b, it can be found that the d-band center of Co and Ni from NC@CL are close to the Fermi level than others, the upshift of d-band center after forming heterojunction can not only improve the conductivity but also promote the interaction between adsorbates and interface.[38]

The differential charge further reveals the electron transfer state between the NC and CL of NC@CL heterostructure. The analysis reveals a reduction in interfacial charge density, as depicted in Figure 7c. This decrement in interfacial charge density results in an improvement in material conductivity, augmentation of heterojunction material stability, and enhancement of charge transport efficiency. As shown in Figure 7c,d, the electrons of NC accumulate at the Co atom and dissipate at the Ni atom. At this point, the Ni atom is activated by Co atom on the NC@CL surface. The differential charge density diagram at the heterojunction interface shows that the O atom becomes the main

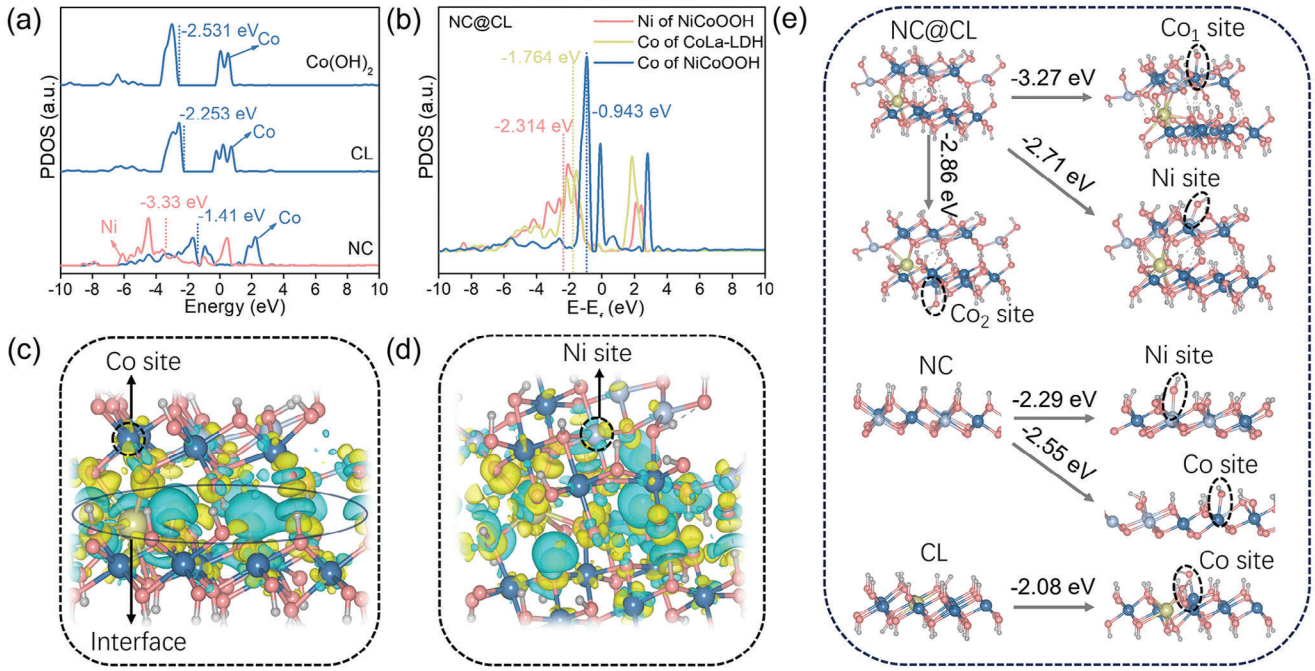

Figure 7. a,b) Partial density of states for $Co(OH)_2$, CL, NC, and NC@CL. c,d) The differential charge density of NC@CL. e) Models of the calculation of OH^- adsorption and the calculated corresponding adsorption energy on different sites of NC@CL.

electron dissipation region at the interface which indicates that the activity of O is greatly improved. Furthermore, charge accumulation is observed at La sites, signifying the activation of adjacent oxygen atoms by La. Analysis with the electron localization function diagram (Figure 3f) suggests that the incorporation of La and its bonding with superior oxygen atoms effectively serves as an electron transport pathway, thereby facilitating accelerated electron conduction.

To further illuminate the excellent capacity performance of NC@CL heterostructure the dynamic process of OH^- ion adsorption/desorption for redox reaction is studied. The adsorption structural models of the above four materials are shown in Figures 7e and S15 (Supporting Information). In general, the electrode material captures the OH^- ions from the electrolyte when it's charged and then undergoes redox reactions to convert into final high-valence product and H_2O.[11b] As for the discharge process, the reactions occur in reverse. Therefore, the adsorption free energy of OH^- on the electrode surface can be used as an ingenious indicator of the redox reaction barrier.[39] The adsorption energy of OH^- in different adsorption sites is calculated by DFT calculation. For NC@CL heterostructure, it was found that the free energy for OH^- adsorption in Co site of NC is -3.27 eV, which is lower than that of Ni site of NC (−2.71 eV) or Co site of CL (−2.86 eV), implying that the optimum OH^- adsorption position is Co site of NC. By comparing the adsorption energy of OH^- in different sites in NC@CL, NC, and CL, it can be found that the NC@CL obtained lower adsorption energy suggesting a more thermodynamically favorable OH^- adsorption/desorption on NC@CL heterostructure.[40] Therefore, the kinetics of the reversible redox reactions on the electrode are significantly accelerated, hence the high rate capability of NC@CL electrode is obtained.

3. Conclusion

In summary, we propose a straightforward strategy for fabricating an NC@CL heterostructure exhibiting exceptional charge storage performance successfully. The hierarchical flower-like array of NC@CL, featuring a high BET surface area, offers abundant active sites conducive to redox reactions. The partial modulation of octahedral sites by lanthanum, along with microscopic stress from the heterojunction, introduces distortions in the NC and CL crystal structures. This enhances the electrochemical properties by fine-tuning the transport pathways and rates of electron and ion transfer, ultimately accelerating the charge transfer process of NC@CL. Furthermore, the interfacial interaction between NC and CL generates numerous active sites, enhancing charge transfer and thus boosting the energy storage performance of NC@CL.This work offers novel insights into the interplay between active sites and reactants, as well as the role of interfacial effects in the mechanism of charge storage reactions.

Supporting Information

Supporting Information is available from the Wiley Online Library or from the author.

Acknowledgements

The authors gratefully acknowledge the financial supported by Hainan Provincial Natural Science Foundation of China (No. 222MS060). The Grants for the Innovation Center of Academician Sun Shigang's Team in Hainan Province.

Conflict of Interest

The authors declare no conflict of interest.

Data Availability Statement

The data that support the findings of this study are available from the corresponding author upon reasonable request.

Keywords

aqueous Zn battery, heterostructure, nanosheets, supercapacitors, transition metal hydroxides

Received: August 12, 2024
Revised: October 18, 2024
Published online:

[1] a) J. Zhang, X. Dong, G. Wang, J. Chen, R. Wang, *Appl. Catal., B* **2024**, *342*, 123459; b) H. Lin, C. Lin, F. Xiao, L. He, P. Xiong, Y. Luo, X. Hu, Q. Qian, Q. Chen, Z. Wen, L. Zeng, *Adv. Funct. Mater.* **2023**, *34*, 2310486.

[2] a) W. Fan, Q. Wang, K. Rong, Y. Shi, W. Peng, H. Li, Z. Guo, B. B. Xu, H. Hou, H. Algadi, S. Ge, *Nano-Micro Lett.* **2023**, *16*, 36; b) A. H. Anwer, M. Shoeb, F. Mashkoor, A. Ali, S. Kareem, M. Z. Ansari, J. M. Park, C. Jeong, *Appl. Catal., B* **2023**, *339*, 123091; c) F. Li, Y.-L. Liu, G.-G. Wang, D. Yan, G.-Z. Li, H.-X. Zhao, H.-Y. Zhang, H.-Y. Yang, *J. Mater. Chem. A* **2021**, *9*, 9675.

[3] S. Cai, J. Hu, Y. Luo, P. Zhu, T. He, G. Zou, H. Hou, X. Ji, *Adv. Funct. Mater.* **2023**, *34*, 2309667.

[4] a) Y. Wang, Y. Gao, J. He, J. Yang, G. Fu, Q. Cao, J. Pu, F. Bu, X. Xu, C. Guan, *Adv. Mater.* **2023**, *36*, 2307819; b) J. Cai, H. Zhang, L. Zhang, Y. Xiong, T. Ouyang, Z.-Q. Liu, *Adv. Mater.* **2023**, *35*, 2303488; c) B.-H. Xiao, R.-T. Lin, K. Xiao, Z.-Q. Liu, *J. Power Sources* **2022**, *530*, 231307.

[5] C. Wang, X. Li, H. Song, P. K. Chu, K. Huo, *Adv. Funct. Mater.* **2023**, *34*, 2311040.

[6] a) R. Gao, D. Yan, D. G. Evans, X. Duan, *Nano Res.* **2017**, *10*, 3606; b) Y. Zhao, H. Lin, M. Chen, D. Yan, *Ind. Eng. Chem. Res.* **2014**, *53*, 3140; c) D. Yan, J. Lu, L. Chen, S. Qin, J. Ma, M. Wei, D. G. Evans, X. Duan, *Chem. Commun.* **2010**, *46*, 5912.

[7] C. Zhang, H. Xing, X. Duan, F. Pan, K.-J. Chen, T. Wang, *Small* **2023**, *20*, 2307795.

[8] H. Wang, M. Liang, Z. Miao, *Chem. Eng. J.* **2023**, *470*, 144148.

[9] M. Liang, X. Li, Y. Kang, N. u. RehmanLashari, X. Zhang, Y. Zhao, H. Wang, Z. Miao, C. Fu, *J. Power Sources* **2022**, *535*, 231486.

[10] a) W. Hu, L. Chen, B. Geng, Y. Song, Z. Wu, Q. Zheng, G. Shan, M. Du, *Chem. Eng. J.* **2023**, *468*, 143694; b) K. M. Amin, K. Krois, F. Muench, B. J. M. Etzold, W. Ensinger, *J. Mater. Chem. A* **2022**, *10*, 12473; c) X. Li, F. Chen, B. Zhao, S. Zhang, X. Zheng, Y. Wang, X. Jin, C. Dai, J. Wang, J. Xie, Z. Zhang, Y. Zhao, *Nano-Micro Lett.* **2023**, *15*, 32; d) J. Fan, H. Zheng, A. Chen, L. Gu, X. Xie, J. Fan, Z. Ding, *Chem. Eng. J.* **2023**, *476*, 146638; e) M. Gao, J. Huang, Y. Liu, X. Li, P. Wei, J. Yang, S. Shen, K. Cai, *Adv. Funct. Mater.* **2023**, *33*, 2305175; f) Y.-L. Liu, C. Yan, G.-G. Wang, F. Li, Q. Kang, H.-Y. Zhang, J.-C. Han, *Nanoscale* **2020**, *12*, 4040.

[11] a) W. Cao, W. Zhao, C. Xiong, Q. Long, N. Chen, G. Du, *J. Energy Storage* **2023**, *64*, 107213; b) J. Zhao, Y. Wang, Y. Qian, H. Jin, X. Tang, Z. Huang, J. Lou, Q. Zhang, Y. Lei, S. Wang, *Adv. Funct. Mater.* **2023**, *33*, 2210238; c) G. Zhang, H. Yang, H. Zhou, T. Huang, Y. Yang, G. Zhu, Y. Zhang, H. Pang, *Angew. Chem., Int. Ed.* **2024**, *63*, 202401903.

[12] a) M. A. Mushtaq, A. Kumar, G. Yasin, M. Tabish, M. Arif, S. Ajmal, W. Raza, S. Naseem, J. Zhao, P. Li, H. G. Ali, S. Ji, D. Yan, *Small* **2024**, *20*, 2310431; b) P. Li, Y. Lin, Z. Qi, D. Yan, *J. Mater. Chem. A* **2023**, *11*, 21078; c) Z. Guo, W. Ye, X. Fang, J. Wan, Y. Ye, Y. Dong, D. Cao, D. Yan, *Inorg. Chem. Front.* **2019**, *6*, 687.

[13] a) Z.-H. Tang, H.-Y. Zeng, K. Zhang, H.-L. Yue, L.-Q. Tang, S.-B. Lv, H.-B. Wang, *Chem. Eng. Sci.* **2024**, *289*, 119865; b) D. Malavekar, S. Pujari, S. Jang, S. Bachankar, J. H. Kim, *Small* **2024**, *20*, 2312179; c) Y.-L. Liu, C. Yan, G.-G. Wang, H.-Y. Zhang, L.-Y. Dang, B.-W. Wu, Z.-Q. Lin, X.-S. An, J.-C. Han, *ACS Appl. Mater. Interfaces* **2019**, *11*, 9984.

[14] J. Li, L. Wang, H. He, Y. Chen, Z. Gao, N. Ma, B. Wang, L. Zheng, R. Li, Y. Wei, J. Xu, Y. Xu, B. Cheng, Z. Yin, D. Ma, *Nano Res.* **2022**, *15*, 4986.

[15] P. Thondaiman, C. Justin Raj, R. Velayutham, A. Marotrao kale, B. Chul Kim, *Chem. Eng. J.* **2024**, *484*, 149508.

[16] a) S. A. Ansari, N. Parveen, M. Al Saleh Al-Othoum, M. O. Ansari, *J. Adv. Res.* **2023**, *50*, 107; b) Z. Hou, J. Yu, X. Zhou, Z. Chen, J. Xu, B. Zhao, W. Gen, H. Zhang, *J. Colloid Interface Sci.* **2023**, *646*, 753.

[17] a) Z. Zhang, Z. Wang, H. Zhang, Z. Zhang, J. Zhou, Y. Hou, P. Liu, B. Xu, H. Zhang, J. Guo, *J. Mater. Chem. A* **2023**, *11*, 4355; b) R. C. Rohit, A. Jenifer, A. D. Jagadale, V. S. Kumbhar, H. Lee, K. Lee, *J. Energy Storage* **2020**, *28*, 101227.

[18] a) P. Simon, Y. Gogotsi, *Nat. Mater.* **2008**, *7*, 845; b) S. Dutta, A. Bhaumik, K. C. W. Wu, *Energy Environ. Sci.* **2014**, *7*, 3574.

[19] K. G. Cho, H. S. Kim, S. S. Jang, H. Kyung, M. S. Kang, K. H. Lee, W. C. Yoo, *Adv. Funct. Mater.* **2020**, *30*, 2002053.

[20] a) K. Zhou, S. Wang, G. Zhong, J. Chen, Y. Bao, L. Niu, *Small* **2022**, *18*, 2202799; b) W. He, S. Wang, Y. Shao, Z. Kong, H. Tu, Y. Wu, X. Hao, *Adv. Energy Mater.* **2021**, *11*, 2003268.

[21] D. Qi, J. Xu, Y. Zhou, H. Zhang, J. Shi, K. He, Y. Yuan, J. Luo, S. Wang, Y. Wang, *Angew. Chem., Int. Ed.* **2023**, *62*, 202307355.

[22] X. Yang, J. Cheng, Y. Xu, H. Li, W. Tu, J. Zhou, *Chem. Eng. J.* **2023**, *472*, 145076.

[23] X. Dou, D. Yuan, X. Liang, K. Song, R. Hu, L. Zhang, J. C. Roy, X. Jiang, H. K. Liu, Y. Dou, L. Yu, *Chem. Eng. J.* **2023**, *468*, 143715.

[24] J. Ning, M. Xia, D. Wang, X. Feng, H. Zhou, J. Zhang, Y. Hao, *Nano-Micro Lett.* **2020**, *13*, 2.

[25] H. Yang, B. Wang, H. Li, B. Ni, K. Wang, Q. Zhang, X. Wang, *Adv. Energy Mater.* **2018**, *8*, 1801839.

[26] a) J. Long, Q. Yao, X. Zhang, H. Wu, Z.-H. Lu, *Appl. Catal., B* **2023**, *320*, 121989; b) X. Fu, Y. Chen, T. Wang, Z. Li, Y. Lei, S. Kawi, *Int. J. Hydrogen Energy* **2022**, *47*, 27996.

[27] a) N. Liu, D. Cao, W. Liu, H. Zhang, Y. Zhu, L. Chang, D. Wu, D. Cheng, *Int. J. Hydrogen Energy* **2022**, *47*, 14504; b) L. Gao, Y. Li, G. Li, J. Huo, L. Jia, *Chem. Eng. J.* **2023**, *451*, 138743.

[28] S. Ni, H. Qu, Z. Xu, X. Zhu, H. Xing, L. Wang, J. Yu, H. Liu, C. Chen, L. Yang, *Appl. Catal., B* **2021**, *299*, 120638.

[29] a) C. Zhou, L. Shan, Q. Nan, J. Zhang, Z. Fan, B. Tang, J. Li, J. Yang, H. Zhang, Z. Kang, X. Tian, X. Shi, *Adv. Funct. Mater.* **2024**, *34*, 2312696; b) C. Li, X. Li, Q. Yang, L. Wu, C. Wang, H. Tian, C. Wang, X. Chen, J. Shao, *Adv. Funct. Mater.* **2024**, *34*, 2315137.

[30] L. Liu, E. Raymundo-Piñero, S. Sunny, P.-L. Taberna, P. Simon, *Angew. Chem., Int. Ed.* **2024**, *63*, 202319238.

[31] T. Zhao, D. Yang, B.-X. Li, Y. Shi, Q. Quan, N. Koratkar, Z.-Z. Yu, *Adv. Funct. Mater.* **2024**, *34*, 2314825.

[32] Q. Bi, X. Hu, K. Tao, *Chem.-Eur. J.* **2023**, *29*, 202203264.

[33] J. Zou, J. Xu, H. Wu, H. Dong, M. Zheng, Z. Li, X. Zeng, J. Huang, *J. Energy Storage* **2023**, *68*, 107736.

[34] D. Lee, J. Kim, D. H. Kim, *J. Energy Storage* **2022**, *54*, 105271.

[35] Y. Zhao, S. Wang, F. Ye, W. Liu, J. Lian, G. Li, H. Wang, L. Hu, L. Wu, *J. Mater. Chem. A* **2022**, *10*, 16212.

[36] J. Sun, Y. Wang, J. Zhou, K. Chen, K. Tao, W. Zhao, L. Han, *Inorg. Chem.* **2022**, *61*, 4283.

[37] R. Wang, C. Xu, J.-M. Lee, *Nano Energy* **2016**, *19*, 210.
[38] a) T. Chen, F. Wang, S. Cao, Y. Bai, S. Zheng, W. Li, S. Zhang, S.-X. Hu, H. Pang, *Adv. Mater.* **2022**, *34*, 2201779; b) S. Huang, W. Zhang, Q. Chen, S. Zhou, L. Sun, L. Sha, G. Zhuang, P. Wang, X. Han, *Chem.-Eur. J.* **2023**, *29*, 202300321.
[39] D. Cai, Y. Wang, B. Fei, C. Chao Li, C. Zhang, B. Sa, Q. Chen, H. Zhan, *Chem. Eng. J.* **2022**, *450*, 138341.
[40] Z. Li, H. Li, J. Song, T. Liu, Y. He, A. Meng, Y. Liu, C. Chen, C. Sun, M. Hu, L. Wang, G. Li, J. Zhao, *Energy Storage Mater.* **2022**, *50*, 252.